Toxoplasma gondii association with host mitochondria requires key mitochondrial protein import machinery

Matthew L. Blank[a], Jing Xia[a], Mary M. Morcos[a], Mai Sun[b], Pamela S. Cantrell[b], Yang Liu[b], Xuemei Zeng[b], Cameron J. Powell[c], Nathan Yates[b,d], Martin J. Boulanger[c], and Jon P. Boyle[a,1]

[a]Department of Biological Sciences, Dietrich School of Arts and Sciences, University of Pittsburgh, Pittsburgh, PA 15261; [b]Biomedical Mass Spectrometry Center, University of Pittsburgh Schools of the Health Sciences, Pittsburgh, PA 15261; [c]Department of Biochemistry and Microbiology, University of Victoria, Victoria, BC, Canada V8P 5C2; and [d]Department of Cell Biology, University of Pittsburgh School of Medicine, Pittsburgh, PA 15261

Edited by Thomas E. Wellems, NIH, Gaithersburg, MD, and approved February 15, 2021 (received for review June 26, 2020)

Host mitochondrial association (HMA) is a well-known phenomenon during *Toxoplasma gondii* infection of the host cell. The *T. gondii* locus *mitochondrial association factor 1* (*MAF1*) is required for HMA and *MAF1* encodes distinct paralogs of secreted dense granule effector proteins, some of which mediate the HMA phenotype (MAF1b paralogs drive HMA; MAF1a paralogs do not). To identify host proteins required for MAF1b-mediated HMA, we performed unbiased, label-free quantitative proteomics on host cells infected with type II parasites expressing MAF1b, MAF1a, and an HMA-incompetent MAF1b mutant. Across these samples, we identified ∼1,360 MAF1-interacting proteins, but only 13 that were significantly and uniquely enriched in MAF1b pull-downs. The gene products include multiple mitochondria-associated proteins, including those that traffic to the mitochondrial outer membrane. Based on follow-up endoribonuclease-prepared short interfering RNA (esiRNA) experiments targeting these candidate MAF1b-targeted host factors, we determined that the mitochondrial receptor protein TOM70 and mitochondria-specific chaperone HSPA9 were essential mediators of HMA. Additionally, the enrichment of TOM70 at the parasitophorous vacuole membrane interface suggests parasite-driven sequestration of TOM70 by the parasite. These results show that the interface between the *T. gondii* vacuole and the host mitochondria is characterized by interactions between a single parasite effector and multiple target host proteins, some of which are critical for the HMA phenotype itself. The elucidation of the functional members of this complex will permit us to explain the link between HMA and changes in the biology of the host cell.

mitochondria | *Toxoplasma gondii* | virulence | tandem gene expansion | neofunctionalization

The association of host cell organelles with their invading pathogens has long been observed, but the intricate molecular mechanisms underlying most of these interactions have remained elusive. For example, the striking cellular phenotype of some pathogens associating with host mitochondria has been phenotypically characterized by microbiologists for quite some time. This phenotype has been reported in *Legionella pneumophila* (1), *Chlamydia psittaci* (2, 3), *Hammondia hammondi* (4, 5), and *Toxoplasma gondii* (4, 6, 7). While the secreted bacterial effector driving association of the infectious *C. psittaci* elementary body with its host mitochondria remains unknown, key mitochondrial functions like adenosine triphosphate (ATP) synthesis and the regulation of glucose metabolism are enhanced upon pathogen infection (8). Additionally, mitochondrial association is specific to *C. psittaci* and this association is absent in both *Chlamydia pneumonia* and *Chlamydia trachomatis* (9). Recent discoveries in *L. pneumophila* answered a decades-long question about the impact of bacterial association with host mitochondria. *L. pneumophila* utilizes the protein effector MitF, and its presence at the legionella-containing vacuole mediates recruitment of the GTPase dynamin 1-like protein (Drp1) to the mitochondrial membrane and induces mitochondrial fission in macrophages (10). Similar work in the eukaryotic parasite *T. gondii* has resulted in the identification of the parasite effectors driving association with host mitochondria (6). *T. gondii* secretes the effector protein mitochondrial association factor 1b (MAF1b) from its dense granules upon invasion and, after trafficking to the parasitophorous vacuole membrane (PVM), it is required for association with host mitochondria (4, 6). This association is physiologically relevant, since host mitochondrial association-positive (HMA+) parasites outcompete their HMA− counterparts during acute infection in mice (4, 7). This growth advantage was first recognized during acute infection, but there is also a MAF1b/HMA-dependent increase in cyst burden in the brain of mice during chronic infection (11). The exact signaling pathways underlying these physiological effects of MAF1b and identification of host proteins required for HMA represent an important means to uncover these mechanisms.

The *MAF1* locus varies in size and gene content between strains and species and these differences are predictive of locus function with respect to HMA in *Neospora caninum*, *H. hammondi*, and *T. gondii* (4). Based on extensive sequence analysis and molecular cloning, we found that the *MAF1* locus in *T. gondii*, which contains 6 to 10 copies dependent on the strain, originated from a single *MAF1* copy (MAF1a), represented in its likely ancestral form in *N. caninum*, which is incapable of driving HMA (4, 12). *T. gondii* type I and type III strains are "HMA-competent" while *T. gondii* type II strains are not (6), and this is due to undetectable expression of *Tg*MAF1b (4, 6). In contrast to *N. caninum*,

Significance

Many pathogens manipulate the host environment to promote their survival and eventual transmission. *Toxoplasma gondii*, an intracellular parasite that can cause disease in those with weakened immune systems, is no exception. One of the more dramatic effects of *T. gondii* infection on the host cell is a relocalization of the host mitochondria around the parasite-containing vacuole. Here, we have identified two host proteins that are required for *T. gondii* manipulation of host mitochondria, both of which are involved in mitochondrial protein import. This discovery is a remarkable example of a parasite gene evolving to specifically target a host receptor on the surface of an organelle.

Author contributions: M.L.B., N.Y., M.J.B., and J.P.B. designed research; M.L.B., J.X., M.M.M., M.S., P.S.C., Y.L., X.Z., and C.J.P. performed research; M.L.B., M.S., P.S.C., Y.L., X.Z., C.J.P., N.Y., and M.J.B. contributed new reagents/analytic tools; M.L.B., J.X., M.M.M., M.S., P.S.C., Y.L., X.Z., C.J.P., M.J.B., and J.P.B. analyzed data; and M.L.B. and J.P.B. wrote the paper.

The authors declare no competing interest.

This article is a PNAS Direct Submission.

[1]To whom correspondence may be addressed. Email: boylej@pitt.edu.

This article contains supporting information online at https://www.pnas.org/lookup/suppl/doi:10.1073/pnas.2013336118/-/DCSupplemental.

Published March 15, 2021.

H. hammondi is HMA-competent and consistent with this it has two tandem copies of *MAF1* (MAF1a and MAF1b) (4). *H. hammondi* MAF1b facilitates HMA whereas its MAF1a paralog does not, suggesting that a neofunctionalization event occurred in a common ancestor of *T. gondii* and *H. hammondi* (13). Recent work using a type I *T. gondii* strain (RH) complemented with either a C- or N-terminally tagged *Tg*RHMAF1b paralog identified constituents of the mitochondrial intermembrane bridging space (MIB) complex as uniquely associating with only the HMA-competent (N-terminally tagged) *Tg*RHMAF1b (14). Here, we exploited *T. gondii* MAF1 functional diversity and a recently developed MAF1b mutant that is incapable of driving HMA to identify host proteins that associate only with HMA-competent versions of MAF1, in this case by complementation of a naturally HMA-deficient type II *T. gondii* strain [ME49 (6, 12)]. Through the use of quantitative mass spectrometry and a focused endoribonuclease-prepared short interfering RNA (esiRNA) knockdown (15) screen, we were able to identify and confirm the importance of an outer mitochondrial membrane receptor (translocase of the outer mitochondrial membrane receptor 70; TOM70) and its chaperone (heat shock protein family A member 9; HSPA9) as being critical for *T. gondii* MAF1b-mediated HMA.

Results

Quantitative Mass Spectrometry Analysis Identified a Network of Potential MAF1b Host Binding Partners on the Mitochondria. Type II *T. gondii* strains (including *Tg*Me49) are HMA-negative and despite having multiple copies of the *TgMAF1RHb1* gene they do not express *Tg*MAF1RHb1 (MAF1b) protein (4, 6). We previously generated three *Tg*Me49 parasite clones based on their ability to mediate HMA: *Tg*Me49:*Tg*MAF1RHb1 (HMA+), *Tg*Me49:*Tg*MAF1RHa1 (HMA−), and *Tg*Me49:*Tg*MAF1RHb1 STYL(438–441)RKYK

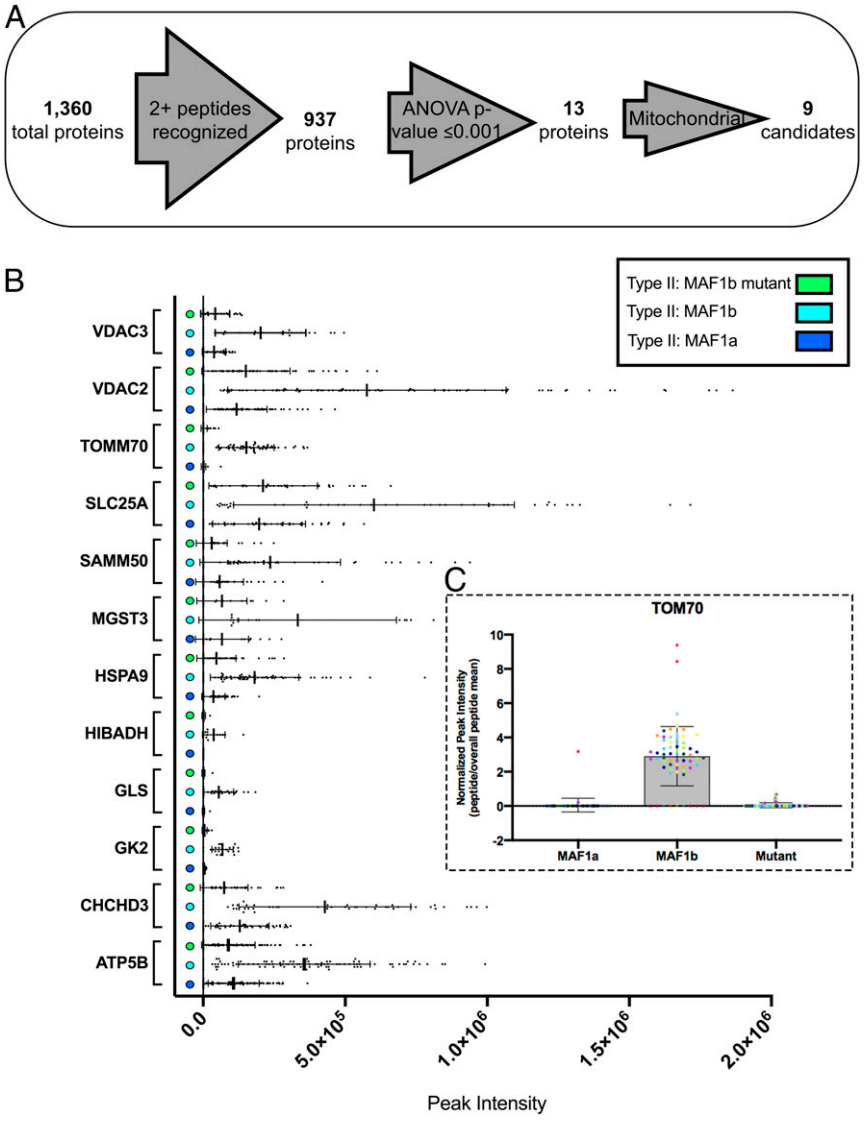

Fig. 1. Quantitative mass spectrometry analysis identified 13 potential MAF1 host binding partners. (*A*) Selection criteria for candidate proteins included identifying proteins with two or more peptide hits and proteins significantly higher in abundance (greater than twofold change) in type II:MAF1b IP samples in comparison with the type II:MAF1a and type II:MAF1b mutant samples and must have an ANOVA *P* value ≤0.001. Nine of the final 13 candidates have a mitochondrial function based on DAVID 6.8 analysis. (*B*) Peak intensity plots for the cumulative ionized peptides from the 13 candidate proteins. All identified peptides for each IP sample ($n = 7$) are graphed against their peak ionization intensity. Error bars indicate SD. (*C*) Normalization of peak intensities for TOM70 cumulative peptide ionizations. Ionization values for each peptide were normalized to overall mean peptide ionization. Each peptide is a different color and each dot represents one of the seven quantitative mass spectrometry replicates. Error bars indicate SD.

(HMA−) (4, 7). Since only *Tg*ME49:*Tg*MAF1RHb1 was capable of driving HMA, yet all three expressed N-terminally hemagglutinin (HA)-tagged MAF1, we infected a monolayer of human foreskin fibroblasts (HFFs) with each parasite clone described above and performed a coimmunoprecipitation assay followed by quantitative mass spectrometry. Prior to analysis and selection of candidate binding partners, we identified a total of 1,360 proteins in our immunoprecipitation (IP) samples (Fig. 1*A*). In order to select candidate proteins, we first excluded proteins that had a single peptide hit, leaving 937 proteins (Fig. 1*A*). Each identified peptide yielded a peak intensity score directly related to its ability to ionize. We hypothesized that proteins required for binding MAF1b at the PVM would be enriched in the *Tg*Me49:*Tg*MAF1RHb1 (type II:MAF1b) samples and less enriched in the *Tg*Me49:*Tg*MAF1RHa1 (type II:MAF1a) and *Tg*Me49:*Tg*MAF1RHb1 STYL(438–441)RKYK (type II:MAF1b mutant) IP samples. For this reason, we then selected candidate binding proteins that had a ≥2-fold change in the type II:MAF1b samples compared with type II:MAF1a and type II:MAF1b mutant and an ANOVA *P* value of <0.001 (Fig. 1*A*). These conditions revealed a final list of 13 candidate binding partners, all of which had multiple peptides showing significant enrichment only in type II:MAF1b pull-downs (*SI Appendix*, Fig. S1*A* and Table S1). Candidate binding partners included proteins required for cellular metabolism including 3-hydroxyisobutyrate dehydrogenase (HIBADH), glycerol kinase 2 (GK2), and ATP synthase F1 subunit beta (ATP5B) (*SI Appendix*, Fig. S1*A* and Table S1). Sorting and assembly machinery component 50 (SAM50), which was previously identified as a potential binding partner of MAF1b, was also significantly enriched in the type II:MAF1b samples (7, 14) (*SI Appendix*, Table S1). Interestingly, proteins known to be enriched at mitochondria–endoplasmic reticulum (ER) contact sites, including TOM70 and HSPA9 (also known as glucose-regulated protein 75; GRP75), were also identified (*SI Appendix*, Table S1). While ranking proteins based on their associated peptide ANOVA *P* values is important for investigating candidates, we also prioritized proteins based on both their degree of variance in raw peak intensity (Fig. 1*B*) and overall scatter of individual peptide ionizations (*SI Appendix*, Fig. S1*A*). These plots illustrated significant variance across targets and between individual peptides derived from those targets (Fig. 1*B*), as well as a variety of ionization intensity profiles across each of the three conditions. For example, while voltage-dependent anion-selective channel 2 (VDAC2) peptides showed high variance and a significant amount of signal under control conditions (MAF1a and mutant pull-downs; Fig. 1*B*), TOM70 showed a much tighter distribution of signal across multiple peptides as well as comparatively low background intensity under control pull-down conditions. Normalizing each peptide ionization intensity to itself further illustrated the low variance for most detected TOM70 peptides (Fig. 1*C*), and a similar pattern was observed for SAM50 (*SI Appendix*, Fig. S1*B*).

Focused RNA Interference Screen Reveals Requirement for TOM70 and HSPA9 in MAF1b-Driven HMA. To identify host proteins required for *T. gondii* binding of mitochondria, we generated esiRNAs (15) to knock down candidate gene expression and assess colocalization of the mitochondria with the PVM. Human U2OS cells were transfected for 48 h with either a target or nontarget esiRNA followed by infection with type II:MAF1b parasites. Knockdown was analyzed using qRT-PCR and candidate transcripts were successfully knocked down between 75 and 95% (Fig. 2*A*). We performed immunofluorescence to stain mitochondria and HA-tagged MAF1b to quantify the percent of HMA+ vacuoles. Vacuoles that were in direct contact with one or more mitochondria were considered HMA+ while vacuoles that showed no colocalization of mitochondria and the vacuole were counted as HMA− (7). To avoid inherent bias in this assay, we blinded each infection condition and counted three replicates ($n = 3$ coverslips per treatment). In vehicle control and control (cytophilin B) esiRNA-treated cells, 76 to 84% of the type II:MAF1b-containing vacuoles were HMA+ (Fig. 2 *B* and *C*). Knockdown of multiple candidates identified in our quantitative mass spectrometry screen, including VDAC2, GLS, GK2, HIBADH, SAM50, and ATP5B, did not significantly reduce HMA efficiency, where again between 71 and 81% of the MAF1b-containing vacuoles were HMA+ (Fig. 2 *B* and *C*). Interestingly, while many of these candidates are key proteins for the structural integrity and function of the mitochondria, only knockdown of ATP5B, a subunit of the multimeric ATPase F1 subunit, resulted in strikingly unhealthy mitochondria. Importantly, even the fragmented bead-like mitochondria in these samples were still clearly associated with the PVM in a MAF1b-dependent manner (Fig. 2 *B* and *C*). Of the nine target proteins screened, TOM70 and HSPA9 esiRNA treatments were the only candidates to significantly reduce the HMA efficiency of the parasites (Fig. 2 *B* and *C*). We validated TOM70 knockdown by comparing TOM70 protein levels between vehicle- and HIBADH esiRNA-treated cells (Fig. 2*D*). TOM70 recognizes key internal mitochondrial targeting sequences in preproteins destined for translocation through the TOM complex (16–18). To confirm that the decrease of HMA was due to TOM70 and not an artifact of disrupting the TOM complex, we knocked down TOM40 transcript, which forms the pore of the complex, and this did not significantly alter HMA (Fig. 2 *B* and *C*). To assess the attenuated HMA phenotype at the ultrastructural level, we infected cells knocked down for either HIBADH or TOM70 with type II:MAF1b parasites and quantified percent vacuole coverage using transmission electron microscopy (TEM). Vacuole coverage in the TOM70 esiRNA-treated cells was significantly lower than both vehicle-treated and HIBADH knockdown cells (Fig. 2*E*, $^{****}P < 0.0001$), further confirming the requirement of the mitochondrial TOM70 receptor in mediating HMA.

Given the clear association between MAF1b and TOM70 following immunoprecipitation and the requirement for host TOM70 for MAF1b-mediated HMA, we wanted to determine if MAF1b interacted specifically and directly with TOM70. After expressing tagged forms of MAF1a (residues 159 to 425) or MAF1b (residues 173 to 443), we incubated them with TOM70 (residues 109 to 598) and observed no evidence for specific or robust direct interactions between MAF1b and human TOM70 (Fig. 2*F*). These data indicate that TOM70 is either not the direct binding partner for MAF1b, or that it binds to MAF1b but only in the presence of other host proteins.

MAF1 Ectopic Expression Validates the Requirement of TOM70 in Mediating Mitochondrial Attachment at the Vacuole. Our esiRNA screen of putative MAF1b-interacting proteins identified TOM70 as being a key mediator of type II:MAF1b-driven interaction with the host mitochondria. To determine if the TOM70 requirement for MAF1b-mediated HMA required other parasite factors, we expressed green fluorescent protein (GFP)-tagged MAF1 in host cells directly. To first assess MAF1 localization and mitochondrial binding, we N-terminally GFP-tagged both *Tg*MAF1RHb1 and *Tg*MAF1RHa1 (MAF1b and MAF1a, respectively) using pcDNA3.1/NT-GFP-TOPO expression. Expression of both GFP-MAF1a and GFP-MAF1b was observed as early as 6 h after transfection and up to 48 h after transfection in U2OS cells (Fig. 3*A*). Strikingly, GFP-MAF1b colocalized with host cell mitochondria as soon as 6 h after transfection and mitochondrial morphology changed dramatically between the 6- and 48-h time points (Fig. 3*A*). Our observations of MAF1b-associated mitochondrial aggregation are consistent with previous work characterizing the ultrastructural changes to the mitochondrial cristae and overall increase in mitochondrial cross-sectional area in vacuole-associated mitochondria but not the remaining free mitochondria within the host cell (4, 7). Importantly, this system not only recapitulated the differential HMA-mediating capacity of

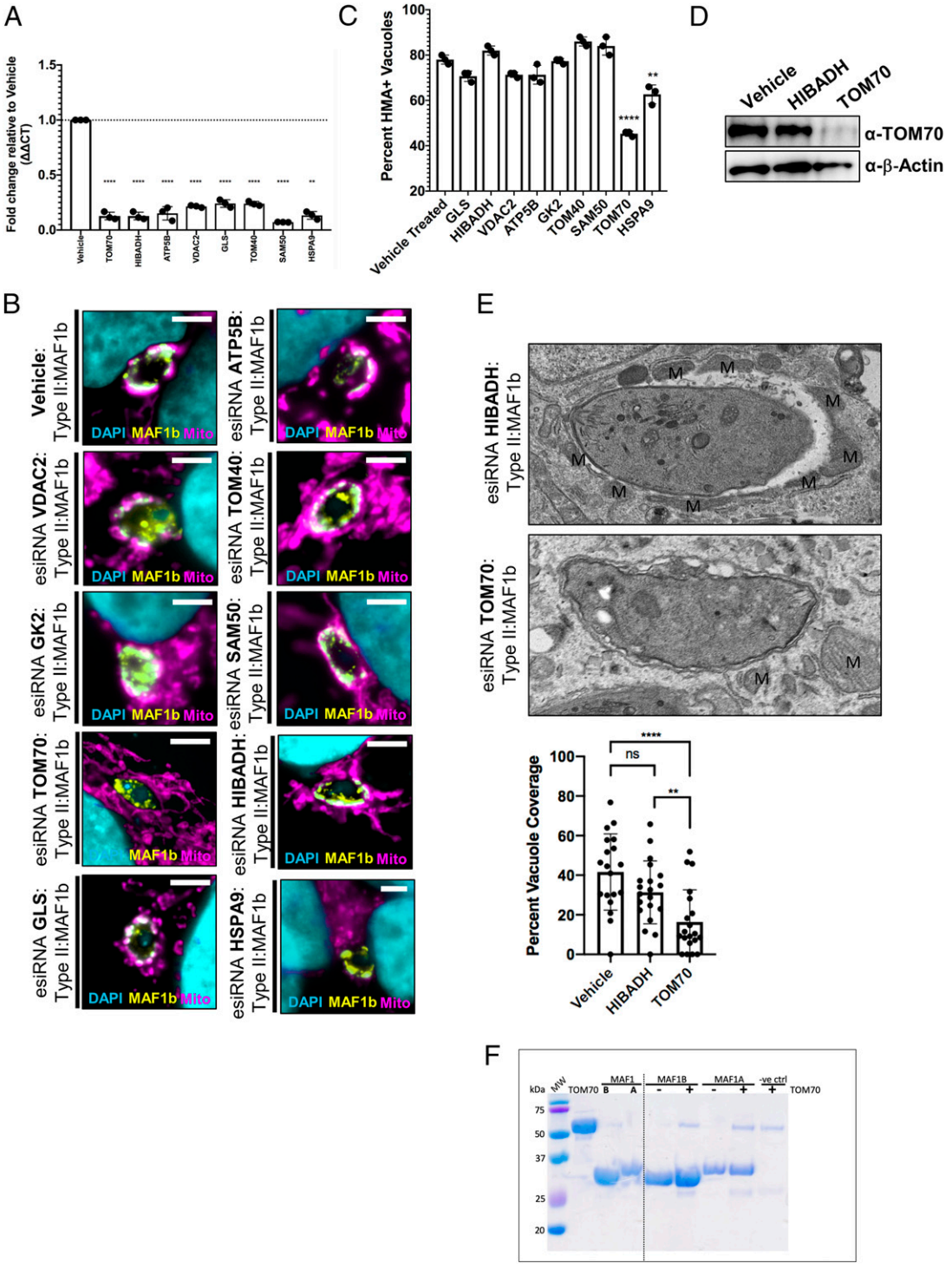

Fig. 2. TOM70 and HSPA9 are required for MAF1b-mediated HMA. (*A*) U2OS cells were treated with 25 nM esiRNA targeting the candidate gene of interest for 48 h followed by type II:MAF1b infection for 24 h (MOI 2). RNA was collected at 48 h and qPCR analysis was performed. $^{**}P = 0.0021$, $^{****}P < 0.0001$, unpaired two-tailed *t* test between cognate vehicle-treated control ΔCT values. Error bars indicate SD. (*B*) U2OS cells were treated as in *A*. Following 48 h of esiRNA treatment, cells were infected for 24 h with type II:MAF1b parasites. Cells were fixed and visualized using fluorescence microscopy. Immunofluorescence staining was performed with antibodies against the HA epitope tag and mitochondria. (Scale bars, 5 μm.) (*C*) HMA+ and HMA− vacuoles were counted ($n = 3$ coverslips per treatment group; 50 vacuoles per coverslip) using fluorescence microscopy. $^{**}P = 0.0013$, $^{****}P < 0.0001$, one-way ANOVA followed by multiple comparisons. Error bars indicate SD. (*D*) U2OS cells were treated as in *A* with 25 nM esiRNA targeting TOM70, HIBADH, or vehicle control, and TOM70 protein levels were measured by Western blot analysis. β-Actin was used as a loading control. (*E*) U2OS cells were treated as in *A* with 25 nM esiRNA targeting TOM70 or HIBADH. After 48 h of treatment, cells were infected with type II:MAF1b parasites for 24 h followed by fixation in 2.5% glutaraldehyde and processed for transmission electron microscopy. For each esiRNA treatment, a minimum of 19 vacuoles were quantified. Mitochondria (M) are labeled. $^{**}P = 0.0055$, $^{****}P < 0.0001$, unpaired two-tailed *t* test; ns, not significant. Error bars indicate SD. (*F*) SDS-PAGE showing results from interaction experiments between recombinant TOM70 (untagged) using 6×His-tagged *Tg*MAF1. No significant MAF1b-specific interactions were observed with TOM70 despite robust expression of each. See text for sizes of each individual recombinant protein which is consistent with their apparent molecular masses on the stained gel.

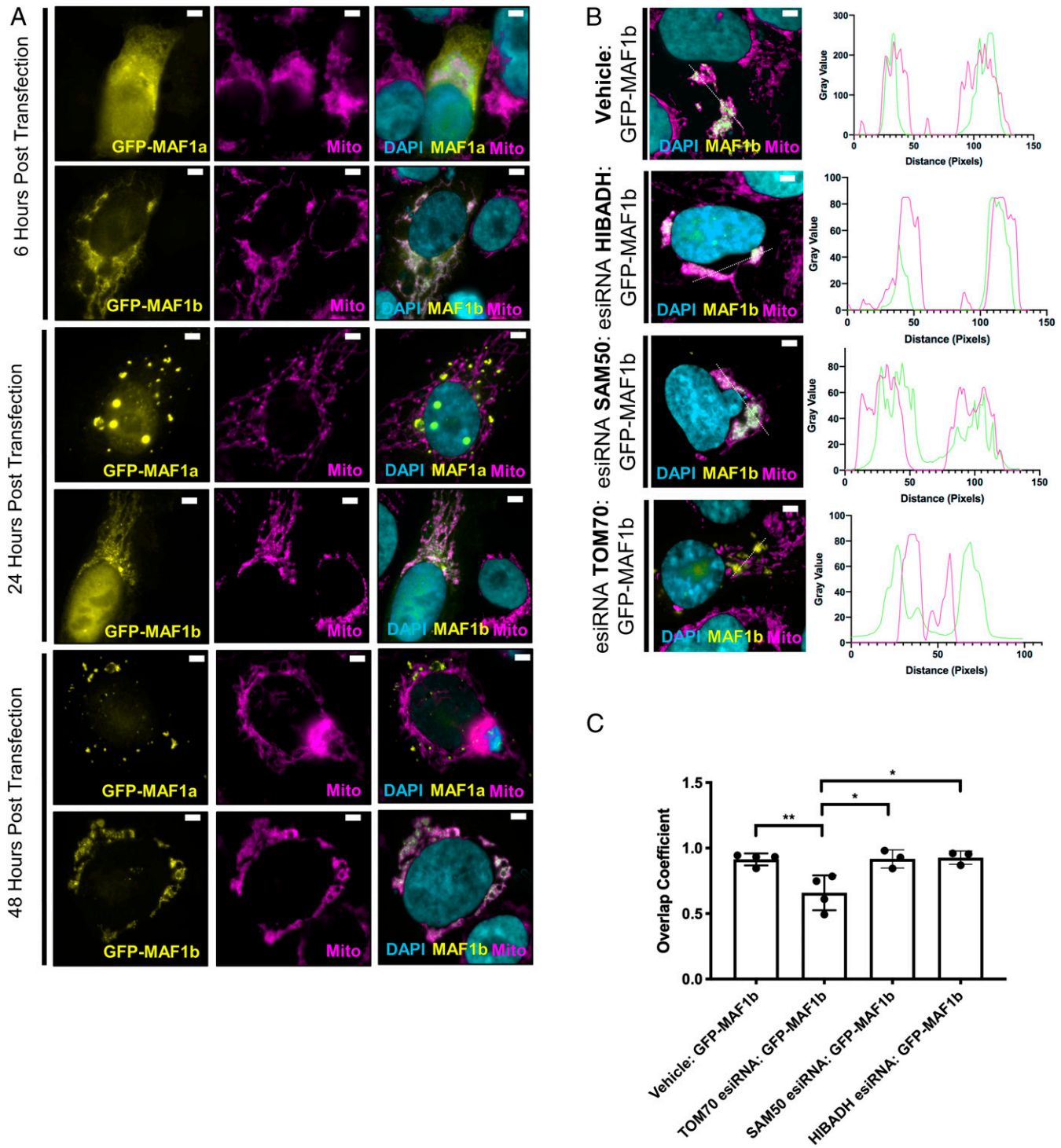

Fig. 3. Ectopic expression of GFP-MAF1b/a confirms the requirement of TOM70 for mediating HMA. (*A*) U2OS cells were transfected with either GFP-MAF1b or GFP-MAF1a. Cells were fixed at either 6 or 8 h after transfection and probed with an antibody against mitochondria. Samples were visualized using epifluorescence microscopy. (*B*) U2OS cells were treated with 25 nM esiRNA against the indicated transcript for 48 h followed by transfection with GFP-MAF1b for 24 h. Cells were fixed and immunofluorescence staining was performed with antibodies against the mitochondria. Profile plots of both the GFP-MAF1b and mitochondria are derived from the dotted white line in the merged image (left to right) to illustrate overlap of signal intensity across each channel. (*C*) Overlap coefficient calculated for each of the esiRNA treatment samples ($n = 4$ images per treatment; representative images in *B*) between the GFP-MAF1b channel and the red (Alexa Fluor 594) channel used to visualize the mitochondria. $^{**}P = 0.0086$, $^{*}P = 0.0101$ (HIBADH), $^{*}P = 0.0127$ (SAM50), one-way ANOVA followed by multiple comparisons. Error bars indicate SD. (Scale bars, 5 μm.)

MAF1a and MAF1b but also confirmed that the C-terminal mutant form of MAF1b is HMA-incompetent in this ectopic expression system [as it is when expressed directly in *T. gondii* (7)]. Specifically, the three MAF1b residues (STL→RKK) required for HMA during parasite infection (7) are also required for MAF1b association with mitochondria during ectopic expression (*SI Appendix*, Fig. S3). These data confirm not only that MAF1b can associate with host mitochondria in the absence of other *T. gondii*-specific factors but also that the mechanism of this interaction is likely to be the same as that which occurs during parasite infection.

Next, we tested MAF1b binding partner candidates from our quantitative mass spectrometry screen for their involvement in mitochondrial localization of GFP-MAF1b. To do this, we knocked down each candidate in U2OS cells using esiRNAs as described above for 48 h, followed by 24 h of GFP-MAF1b expression by lipofection. Neither HIBADH nor SAM50 knockdown disrupted GFP-MAF1b mitochondrial localization (Fig. 3*B*). In contrast, expression of GFP-MAF1b after TOM70 knockdown gave markedly different results, with TOM70 knockdown cells having severely impaired GFP-MAF1b colocalization with mitochondria (Fig. 3*B*). We confirmed this observation quantitatively by measuring the overlap coefficient between MAF1b-GFP and the mitochondria (19), and found that TOM70 knockdown significantly reduced the number of pixels where MAF1b-GFP and mitochondria-derived fluorescent signal colocalized (Fig. 3*C*). These data further confirm the requirement of TOM70 to mediate MAF1b binding to the mitochondria (Fig. 3*C*) during ectopic expression, while we could not demonstrate a requirement for SAM50 using this same approach (Fig. 3 *B* and *C*).

Because TOM70 recognizes and binds internal mitochondrial targeting sequences (iMTSs) on preproteins destined for the mitochondria, we investigated potential iMTSs in both MAF1a and MAF1b (*SI Appendix*, Fig. S3*A*). MAF1 chimeric constructs containing predicted iMTSs from either MAF1b or MAF1a were designed in an effort to identify which iMTS regions were directly required to mediate HMA (*SI Appendix*, Fig. S3*A*). These results revealed a range of HMA phenotypes and suggest the requirement of almost all of the predicted iMTSs to facilitate HMA (*SI Appendix*, Fig. S3*B*).

TOM70 Is Enriched at the Parasitophorous Vacuolar Membrane. Since most of the MAF1b binding candidates have a known mitochondrial function (*SI Appendix*, Table S1), fluorescently labeling a potential binding partner only confirms MAF1b localization to the mitochondria but does not specifically delineate colocalization of that specific protein with MAF1b. We hypothesized that the requirement of TOM70 for HMA would suggest localization of TOM70 on the PVM which could be detected using epifluorescence microscopy. To test this, we measured TOM70 raw intensity values following infection with either type II:MAF1b or type II:MAF1a parasites (Fig. 4*A*). Following a 24-h infection, we stained infected mito-RFP (red fluorescent protein) normal rat kidney (mito-RFP NRK) cells with a TOM70 antibody. TOM70 was significantly enriched at the MAF1b–PVM interface in comparison with unattached mitochondria (Fig. 4 *A* and *B*). TOM70 was also significantly more enriched than the mitochondrial matrix-localized RFP indicator at the MAF1b–PVM interface (Fig. 4 *A* and *B*). This enrichment is lost in the type II:MAF1a-infected cells where we saw no enrichment of RFP-mitochondria or TOM70 at the PVM (Fig. 4 *A* and *C*). The enrichment of TOM70 at the vacuole could be explained by up-regulation and/or stabilization of the protein in cells infected with type II:MAF1b parasites. We wanted to address this question by infecting U2OS cells with either type II:MAF1b or type II:MAF1a parasites followed by Western blot analysis to assay overall TOM70 protein levels. There was no significant change in TOM70 abundance between infection conditions, suggesting no difference in stabilization of TOM70 between MAF1a and MAF1b (Fig. 4 *D* and *E*). However, to determine if TOM70 enrichment at the vacuole was unique to TOM70 and not a more generalized artifact of MAF1b-driven accumulation of mitochondria at the vacuole, we examined another MAF1b candidate binding protein, VDAC2. This voltage-dependent anion channel is predominantly located in the outer mitochondrial membrane and is part of the VDAC family of proteins required for shuttling metabolites into the mitochondria (20, 21). VDAC2 localized at the mitochondria as well as throughout the cytoplasm in both the type II:MAF1b- and type II:MAF1a-infected cells (Fig. 4*F*). Quantification of VDAC2 raw intensity levels at the mitochondria versus in the cytoplasm indicated no VDAC2-specific enrichment at the vacuole in both MAF1b and MAF1a infection conditions (Fig. 4 *G* and *H*). Overall, we were able to identify TOM70-specific enrichment in the regions of the vacuole where MAF1b localizes, suggesting a binding partner complex requiring TOM70. The high concentration of MAF1b/TOM70 at the vacuolar membrane along with the quantitative mass spectrometry data showing the enrichment of mitochondria-specific proteins with MAF1b suggests a preference for mitochondrial binding to the PVM over other host organellar associations like the ER (22). To investigate this preference, we infected U2OS KDEL-mCherry cells with both type II:MAF1b and type II:MAF1a parasites. We found the mitochondria outcompete for contact with the PVM in regions where MAF1b and not MAF1a is deposited (Fig. 5*A*), and these data are consistent with TEM revealing the exclusion of the ER from the space between the vacuolar membrane and the mitochondria (Fig. 5*B*). Taken together, these data confirm the preferential and tight association of MAF1b with the mitochondria that either prevents ER association with the PV or is able to replace the ER as the primary organelle associated with the vacuole in HMA+ strains.

Discussion

The *MAF1* locus has undergone significant gene expansion-driven diversification and type I *T. gondii* maintains seven tandem MAF1 copies in its genome (4, 13, 23). Based on the predicted primary sequence of each MAF1 protein product, these *MAF1* copies can be categorized as either MAF1a or MAF1b paralogs (4). Both paralog types traffic to the PVM upon expression in type II (HMA−) parasites, but only MAF1b drives association of the type II PV with host mitochondria (4). We leveraged the diversity of the *MAF1* locus to identify host proteins required for MAF1b-mediated HMA. We compared interactions between three parasite clones (MAF1b, MAF1a, and a nonfunctional MAF1b) with their host proteins. Through the use of quantitative mass spectrometry, we identified 13 candidate MAF1b host binding proteins. Some of these candidates including IMMT and SAM50 were previously identified as MAF1b binding partners (14).

Here we have shown the requirement of the outer mitochondrial membrane receptor protein TOM70 and mitochondria-specific chaperone HSPA9 in mediating MAF1b binding to the host mitochondria. While both proteins are required for HMA, these data do not exclude the possibility of additional candidates being required to complex together and facilitate MAF1b–mitochondrial binding. It is also not known if the vacuolar localization of MAF1b depends to some extent on host TOM70, which we anecdotally observed in some vacuoles from parasite-infected cells after TOM70 knockdown (as in Fig. 2*B*). TOM70 is a receptor protein and member of the translocase of the outer membrane (TOM) complex (24–26). Collectively, the TOM complex is required for recognition and transport of mitochondria-trafficked proteins (17, 18). While decades of work focus on the TOM20 receptor and the translocase activity of the TOM complex, recent discoveries shed light on the requirement of TOM70 for maintaining mitochondrial health, dynamics, and calcium homeostasis and to impact immunity (27–30). One function of TOM70 is to bind premitochondrial proteins containing internal mitochondrial

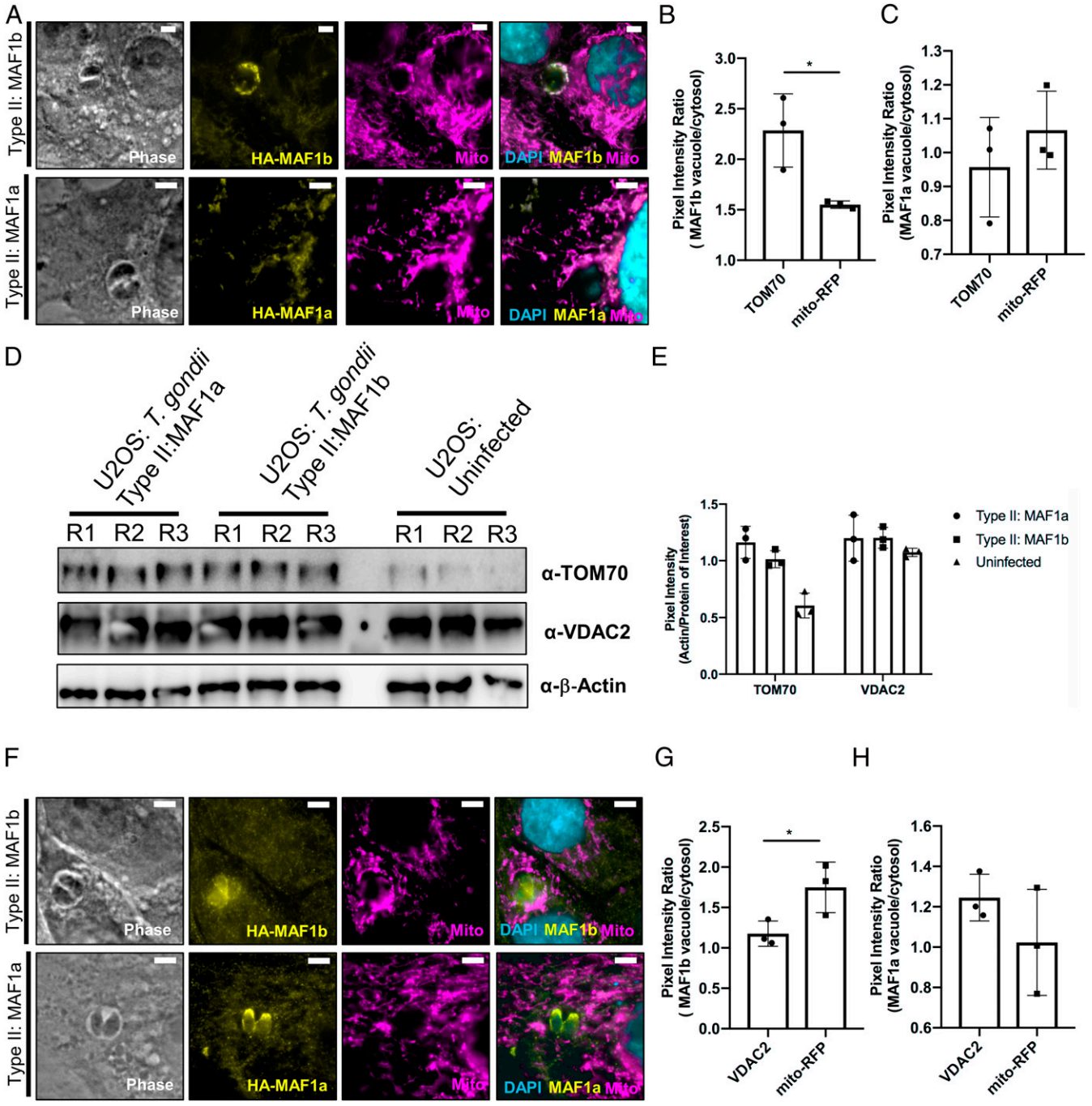

Fig. 4. TOM70 is enriched and redistributed at the parasitophorous vacuole membrane. (*A*) Normal rat kidney cells expressing RFP-labeled mitochondria were infected with type II:MAF1b or type II:MAF1a parasites. Cells were fixed and visualized with epifluorescence microscopy. Immunofluorescence staining was performed with antibodies against TOM70. (*B*) Enrichment of either RFP-mitochondria or TOM70 at the parasitophorous vacuole was performed by quantifying pixel intensity of either the TOM70 or the mitochondria channel in a selected region on the vacuole membrane and a region off of the vacuole membrane. The ratio of these two areas was then calculated to measure enrichment of mito-RFP or TOM70 protein at the type II:MAF1b vacuole. $*P = 0.0250$, unpaired two-tailed *t* test. (*C*) Similar to *B*, enrichment ratios were calculated in cells infected with type II:MAF1a parasites. (*D*) U2OS cells were infected with type II:MAF1b or type II:MAF1a parasites for 24 h (MOI 2) in triplicate. Cells were lysed at 24 h in IP lysis buffer and boiled in lithium dodecyl sulfate sample buffer. Western blot analysis was performed with the listed primary antibodies and HRP-conjugated secondary antibodies. (*E*) Densitometric actin/TOM70 quantification of Western blots depicted in *D* using FIJI ImageJ software (NIH). (*F*) MitoRFP NRK cells were treated as in *A* and immunofluorescence staining was performed with antibodies against VDAC2. (*G*) VDAC2 raw pixel intensity values were measured as previously described in *B* and *C*. $*P = 0.0470$, unpaired two-tailed *t* test. (*H*) Similar to *G*, enrichment ratios were calculated in cells infected with type II:MAF1a parasites. Error bars in *B*, *C*, *G*, and *H* indicate SD. (Scale bars, 5 μm.)

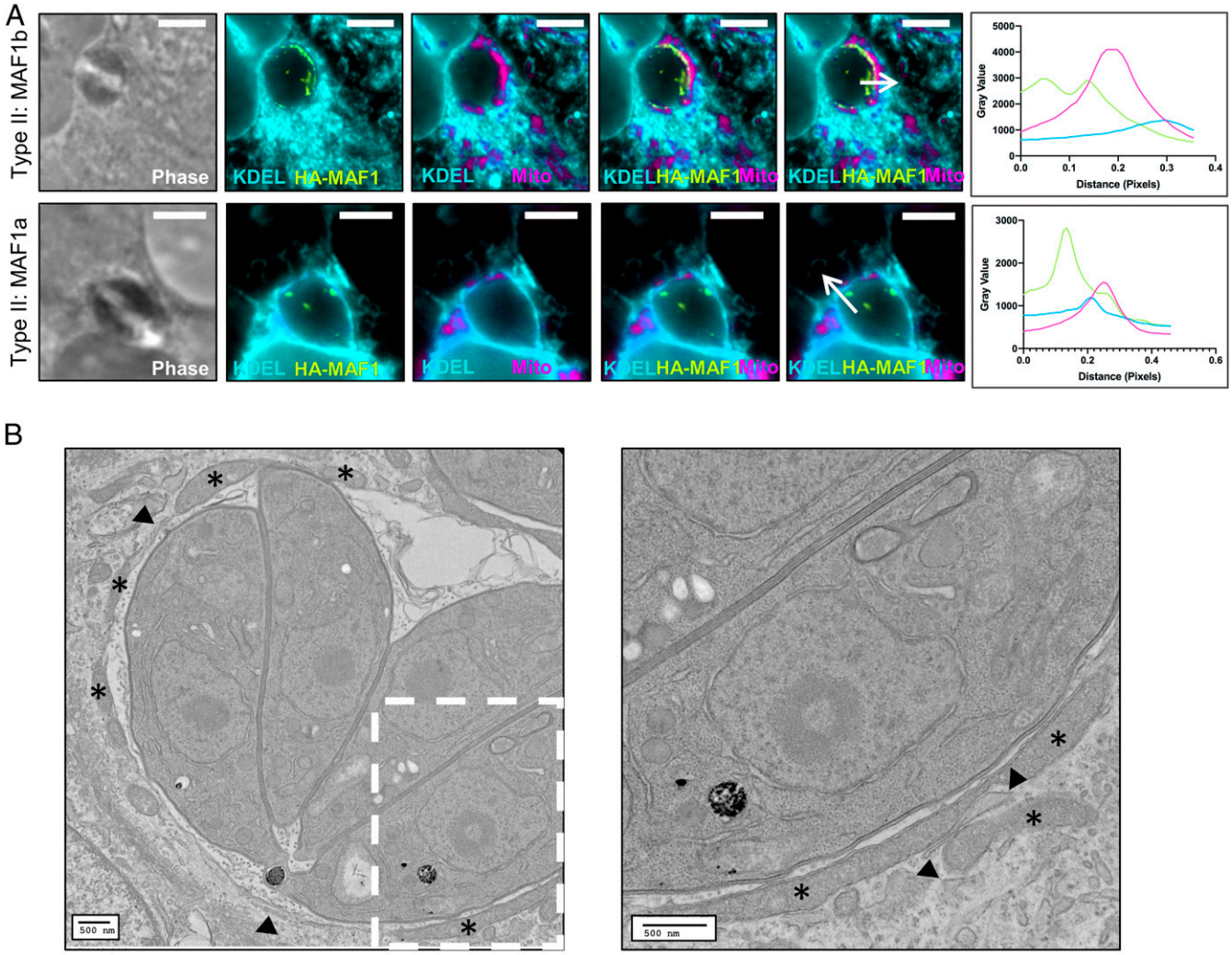

Fig. 5. MAF1b preferentially binds mitochondria and excludes the ER. (*A*) mCherry-KDEL cells were infected with either type II:MAF1b or type II:MAF1a parasites. Cells were fixed 24 hpi and visualized using fluorescence microscopy. Immunofluorescence staining was performed with antibodies against the mitochondria and HA epitope tag. Profile plots of HA-MAF1b (yellow), KDEL (cyan), and mitochondria (magenta) correlate to the arrow in the merged image. (Scale bars, 5 μm.) (*B*) TEM micrograph of HFFs infected with type III (HMA+) parasites. Arrowheads indicate the ER and asterisks indicate mitochondria. (*B*, *Right*) Image is a magnified region of *Left* (dashed square).

targeting sequences through a binding groove (17, 18, 31). Upon binding to TOM70, preproteins are threaded through the TOM40 pore into the inner-membrane space (17, 24). Many of these proteins are destined for SAM50, which is known to interact with TOM70 (32). Previous work identified SAM50 along with MIB complex members as putative binding partners for MAF1b (14). However, using a slightly different experimental strategy with a different strain type, our data show that TOM70 is required for MAF1b-mediated HMA and MAF1b–mitochondrial association, while SAM50 is not.

Additionally, TOM70-specific substrates are targeted to TOM70 through the Hsp70 family of chaperone proteins, specifically HSPA9 (GRP75; mortalin) (33). HSPA9 was also significantly enriched in *Tg*RHMAF1b pull-downs compared with *Tg*MAF1a or the MAF1b mutant was required for HMA based on esiRNA knockdown. While HSPA9 is most notably characterized as a protein found within the mitochondrial matrix responsible for iron–sulfur complex assembly (34), HSPA9 is known to associate with multiple members of the MICOS and MIB complexes, including TOM70 (35). In addition to their more traditional roles in mitochondrial protein translocation, TOM70 and HSPA9 also cluster at mitochondria–ER contact sites formerly known as mitochondria-associated membranes which are implicated in ER–mitochondrial calcium transfer, autophagy signaling, mitochondrial metabolism, and immune signaling (26, 29, 30, 36, 37). Therefore, MAF1b binding to HSPA9 and/or TOM70 could disrupt these mitochondria–ER contact sites and downstream signaling, leading to changes in host responses to infection. Overall, these data identify both TOM70 and HSPA9 as essential host proteins for MAF1b binding and TOM70 enrichment at the PVM. These interactions may suggest manipulation of the mitochondria–ER interface and contribute to parasite in vivo fitness.

The esiRNA knockdown experiments are difficult to perform because we are measuring HMA competency following an extended period of transcript depletion. During all knockdown experiments, we made sure to note any observed changes in mitochondrial morphology and overall cellular health. For example, the candidate protein ATP5B is an essential component of the F1/F0 ATP synthase machinery. Previous literature shows that RNA interference (RNAi) knockdown of ATP5B leads to a decrease in cellular respiratory rate, increased production of reactive oxygen species, and initiation of cellular apoptosis (38, 39). While

fragmented mitochondria were visualized in these samples, type II:MAF1b parasites were still capable of driving clear association with the fragmented mitochondria, indicating the robustness of the HMA phenotype and the tight interaction between MAF1b and the mitochondria. Additionally, in our experiments, knockdown of the previously identified MAF1b-interacting host protein SAM50 did not disrupt HMA. Previous work reports MAF1b interacts with members of the MIB complex including SAM50, IMMT, CHCHD3, and mitofilin (14). The authors hypothesized that because SAM50 is the only member of the complex exposed to the cytosol, this is the reasonable point of contact with MAF1b (14). They found that upon RNAi knockdown of the outermost member, SAM50, and an internal candidate, mitofilin (also called MIC60), the percent of HMA+ vacuoles in both treatments decreased by 40 to 50% (14). While in our study we did not observe any reduction in HMA after SAM50 knockdown, it is possible that we did not knock SAM50 transcript down sufficiently to observe an impact on HMA, even though transcript abundance for all of our targeted genes was reduced by >80% and SAM50 knockdown was very efficient based on qPCR (Fig. 3*A*). There are also strain differences that might account for these divergent results as well. Parasite clones used in Kelly et al. (14) were an HMA+ type I strain with an N-terminally HA-tagged MAF1b paralog and an HMA− type I strain with a C-terminally HA-tagged MAF1b paralog (6, 14). The presence of the C-terminal HA tag functions as a dominant-negative and renders the parasites HMA-incompetent. Our work utilized a different approach by comparing a type II strain complemented with MAF1 paralogs having natural differences in their ability to drive HMA (MAF1b:HMA+ and MAF1a:HMA−), as well as an engineered MAF1b mutant that we showed previously was HMA-incompetent (7). Since MAF1 is a complex locus containing a tandem gene array that varies in copy number and content between strains and even members of the same clonal lineage (4, 13), it is also possible that slight differences in locus content as well as the genetic manipulations used in the strains in our study compared with Kelly et al. underlie these experimental discrepancies. It is worthy of note, however, that despite this difference in SAM50 dependence, both our study and that of Kelly et al. identified many of the same MIB complex proteins as being putative binding partners of MAF1b. These included proteins known to at least transiently interact with TOM70 such as SAM50 and IMMT (32), highlighting a role for TOM70 and the proteins that it interacts with in how MAF1b mediates HMA.

The requirement of TOM70 in mediating HMA is also confirmed by ectopic overexpression. The purpose of this method is to assay MAF1b interactions without the milieu of parasite effectors and subsequent pathway manipulations in a parasite infection. N-terminally GFP-tagged MAF1b traffics directly to the host mitochondria as early as 6 h after transfection (Fig. 3*A*). This is in direct contrast to the GFP-tagged MAF1a which remains cytosolic and occasionally forms puncta in both the cytosol and nucleus. Interestingly, overexpression of GFP-MAF1b in the host cell causes dramatic aggregation of the mitochondria which is not observed following GFP-MAF1a expression. Additionally, these morphological changes to the mitochondria are not seen in the cells knocked down for TOM70 followed by GFP-MAF1b expression.

We observed a significant enrichment of TOM70 at the MAF1b–mitochondrial interface and, using immunofluorescence, we were able to quantify the significant enrichment of TOM70 at the vacuole in comparison with a mito-RFP mitochondrial marker, suggesting possible aggregation or stabilization of TOM70 at the regions on the vacuole in contact with MAF1b. In mammalian cells, TOM70 clusters at specific ER–mitochondrial contact sites and recruits ER-bound inositol triphosphate receptor (IP3R3) and HSPA9 to transfer Ca^{2+} from the ER to the mitochondria (26). This ER–mitochondrial contact site mechanism is essential for maintaining healthy mammalian cell homeostasis and mitochondrial health (26). When TOM70 is knocked down, the ER–mitochondrial transfer of Ca^{2+} is ineffective and the cells show a marked increase in autophagy and decreased proliferation (26). Additionally, the attachment of the host mitochondria to the vacuole excludes the ER along the entire length of the interface, a phenomenon which we observed using both epifluorescence and TEM (Fig. 5). ER associations with the *T. gondii* PV have been described previously (22, 40, 41) but our data indicate that there is a trade-off between MAF1b-driven HMA and vacuolar ER association. Moreover, by interfacing with the HSPA9–TOM70 complex, MAF1b may impact mitochondrial function and signal cellular autophagy leading to improved *T. gondii* growth conditions, and some of these effects could be due to differences in the amount of mitochondrial versus ER association with the PV. *L. pneumophila* utilizes a similar mechanism where bacterium induction of mitochondrial fragmentation leads to impairment of oxidative phosphorylation and Warburg-like metabolism promoting bacterial replication (10). In the case of *T. gondii*, these conditions would describe the increase in parasite fitness in both acute and chronic in vivo infections.

In summary, by leveraging the natural sequence diversity of an expanded and diversified *T. gondii* locus, we identified the requirement of the host proteins, TOM70 and HSPA9, in mediating host mitochondrial association. These findings shed light on the intricate host–pathogen molecular arms race for pathogen manipulation of host organelles.

Materials and Methods

Molecular Methods. All primer sequences are listed in *SI Appendix*, Table S2.

Parasite Expression of MAF1 Paralogs and Transgenic Parasites. Parental plasmid (pATTGra_HA_HPT) for expression of *Tg*MAF1RHb1 (MAF1b) and *Tg*MAF1RHa1 (MAF1a) paralogs contained the selectable HXGPRT gene marker. Transgenic clones were generated using type II *Tg*Me49ΔHXGPRT:luciferase parasites that were transfected by electroporation at 1.6 Kv and 25 μF with 50 μg of pATTGra *Tg*MAF1RHb1 (MAF1b) and *Tg*MAF1RHa1 (MAF1a) linearized with HindIII. *Tg*Me49ΔHXGPRT:luciferase parasites were scraped and passed through a 25- and 27-gauge needle. Cell lysate was centrifuged for 10 min at 800 × *g* and 2 × 107 parasites were resuspended in Cytomix (120 mM KCl, 0.15 mM $CaCl_2$, 10 mM KPO_4, 25 mM Hepes, 2 mM ethylenediaminetetraacetate [EDTA], 5 mM $MgCl_2$, pH 7.6), ATP, and glutathione. Parasites were selected with mycophenolic acid/xanthine and cloned by limited series dilution in a 96-well plate. Positive and negative parasite clones were confirmed through immunofluorescence analysis by the presence or absence of an HA tag. *Tg*Me49:*Tg*MAF1RHb1 (RHb1 clone 1, i.e., "type II:MAF1b"), *Tg*Me49:*Tg*MAF1RHa1 (RHa1 clone 3, i.e., "type II:MAF1a"), and *Tg*Me49:empty vector (EV clone 1) were passage-matched and used for the entirety of all experiments. Additionally, *Tg*Me49:*Tg*MAF1RHb1 STYL(438–441) RKYK clone 6 (STYL/RKYK clone 6, i.e., "type II:MAF1b mutant") was similarly generated and used for all experimentation.

GFP-MAF1b/a constructs were generated using the pcDNA3.1/NT-GFP-TOPO GFP-fusion TOPO TA Expression Kit (Thermo Fisher). The region of MAF1b/a cloned into the pcDNA3.1 expression plasmid excluded the first 23 residues containing the signal peptide. MAF1b (residues 24 to 446) and MAF1a (residues 24 to 446) were PCR-amplified and gel-purified prior to GFP fusion.

MAF1 chimeras 1, 3, and 4 were generated using overlapping PCR and Gibson assembly (NEB Gibson Assembly Master Mix) methods. MAF1 chimera 2 was generated using a site-directed mutagenesis kit (NEB Q5 Kit) to mutate both MAF1a iMTS3 and the C-terminal residues (STYL→RKYK). The same C-terminal residue changes (STYL→RKYK) were made in MAF1 chimera 1 using the same site-directed mutagenesis methods.

Cell Maintenance and Parasite Infection. All *Tg*Me49 parasite clones were routinely passaged in human foreskin fibroblasts (HFFs) and incubated at 37 °C in 5% CO_2. Following parasite selection and cloning, all HFFs were incubated in Dulbecco's modified Eagle's medium supplemented with 10% fetal bovine serum, 2 mM glutamine, and 50 μg/mL penicillin and streptomycin (cDMEM). Human bone osteosarcoma (U2OS), U2OS-KDEL-mCherry, and NRK mito-RFP (42) cells were also routinely passaged in cDMEM. All experimental parasite infections included scraping and passing cell lysate

MICROBIOLOGY

through a 25- and 27-gauge needle followed by counting on a hemocytometer and infection at the noted multiplicity of infection (MOI).

Complementary DNA Synthesis and qPCR/TOM70 Protein Knockdown Analysis. After 48 h after 25 nM esiRNA treatment, three wells were lysed using the Qiagen RNA Shredder and RNeasy RNA Extraction Kit. RNA samples were reverse-transcribed using the SuperScript III Reverse Transcriptase protocol (Thermo Fisher) and qPCR was performed using SYBR Green Supermix (Bio-Rad). Quantification and statistical analyses were performed in Prism (GraphPad). Replicate cycle threshold (CT) values were used to determine statistical significance in Prism. Additionally, vehicle, TOM70, and HIBADH esiRNA-treated wells were lysed in Pierce IP lysis buffer (Thermo Fisher) and treated with cOmplete protease inhibitors (Roche) on ice. Samples were boiled in SDS sample buffer for 10 min, resolved by 10% sodium dodecyl sulfate-polyacrylamide gel electrophoresis (SDS-PAGE), and transferred to a nitrocellulose membrane. Membranes were blocked in 5% bovine serum albumin (BSA) in phosphate-buffered saline with Tween 20 (PBST) and probed with primary antibodies to TOM70 and β-actin followed by horseradish peroxidase (HRP)-conjugated secondary antibodies. Membranes were visualized with SuperSignal West Femto chemiluminescent substrates. Antibodies used for these experiments were as follows: anti-TOM70 (sc-390545; Santa Cruz Biotechnology), anti–β-actin (4970; Cell Signaling Technology), goat anti-rabbit immunoglobulin G (IgG) HRP (Southern Biotech), and goat anti-mouse IgG HRP (Southern Biotech). Blots were imaged on a 600 RGB imager from Amersham Biosciences using chemiluminescence settings.

esiRNA Generation and RNAi Treatment. Silencing regions (400 to 600 bp) of a candidate gene were PCR-amplified to include a 5′ and 3′ T7 RNA polymerase promoter sequence (forward 5′-TAATACGACTCACTATAGGGAGAG-3′, reverse 5′-TAATACGACTCACTATAGGGAGAC-3′) from human embryonic kidney cell complementary DNA. PCR products were gel-purified and Sanger sequencing confirmed candidate sequences (Genewiz); 250 ng of verified product was in vitro transcribed using components of the MEGAscript T7 Kit. Following DNase treatment, transcribed RNA product was digested with RNase III for 2 h at 37 °C. Digested esiRNA products were purified by passing the solution in equilibrium buffer (20 mM Tris·Cl, 1 mM EDTA, and 300 mM NaCl) through Q-Sepharose beads followed by wash buffer (20 mM Tris·Cl, 1 mM EDTA, and 400 mM NaCl). Purified product was eluted off the beads in elution buffer (20 mM Tris·Cl, 1 mM EDTA, and 520 mM NaCl). Eluted esiRNA precipitated overnight in isopropanol and was resuspended in 50 μL of nuclease-free H_2O.

U2OS cells were seeded in a 24-well plate at 37 °C in 5% CO_2 for 24 h to reach 80% confluency. Six wells for each candidate gene were treated with 25 nM esiRNA using DharmaFECT-1 reagent for 48 h. Three wells were infected with type II:MAF1b parasites (MOI 2) and the remaining wells were lysed for RNA extraction and purification. Cells were fixed at 24 h postinfection (hpi) with 4% formaldehyde in PBS followed by immunofluorescence analysis (see below).

HMA Quantification post RNAi Treatment. Following RNAi treatment and 24-h infection with type II:MAF1b parasites (MOI 2), cells were fixed with 4% formaldehyde in PBS. Immunofluorescence staining with anti-mitochondria (ab92824; Abcam) and anti-HA rat monoclonal antibody (3F10 clone; Roche) was performed and vacuoles were scored as either HMA+ or HMA− vacuoles (50 vacuoles quantified, $n = 3$) using epifluorescence microscopy. Vacuoles showing colocalization of HA-MAF1b with at least one mitochondrion were scored as HMA+, while all others were scored as HMA−. The percent of the HMA+ was tallied for each of the three biological replicates.

Immunofluorescence. HFFs and U2OS cells, U2OS cells expressing KDEL-mCherry (43), and NRK mito-RFP cells (42) were grown in cDMEM on glass coverslips in a 24-well plate. KDEL-mCherry cells were provided by Carolyn Coyne, Department of Pediatrics, University of Pittsburgh School of Medicine. Following either esiRNA knockdown, GFP-MAF1a/b expression, or type II:MAF1a/b infection, cells were fixed with 4% paraformaldehyde for 15 min and permeabilized with 0.1% Triton X-100 in PBS at room temperature. Cells were then probed with primary antibodies diluted in PBS for 1 h at room temperature while shaking. Following PBS washes, cells were incubated in secondary antibodies fused to a fluorescence indicator for 1 h at room temperature while shaking (Life Technologies; Alexa Fluor H+L) followed by PBS washes. Cells were mounted on glass slides using ProLong Diamond Antifade Mountant (Thermo Fisher) and cured in the dark for 24 h. Immunofluorescence primary antibodies used in this work include anti-HA rat monoclonal antibody (3F10 clone; Roche), anti-mitochondria (ab92824; Abcam), anti-TOM70 (sc-390545; Santa Cruz Biotechnology), and anti-VDAC2 (PA5-28106; Thermo Fisher). Images were taken of up to five total channels depending on the experiment: 488, 594, 647, and 350 nm and differential interference contrast/phase using an Olympus IX83 inverted microscope equipped with a 100×/1.65 numerical aperture oil-immersion objective and DAPI, fluorescein isothiocyanate, Texas red, and far red filter sets. Images were cropped and merged using FIJI ImageJ (NIH). A single postprocessing step was performed in Adobe Photoshop using the "selective color change" option to make the images accessible to those with color blindness (green converted to yellow, blue converted to cyan, and red converted to magenta).

TEM and Percent Vacuole Coverage Quantification. U2OS cells were treated with 25 nM vehicle, TOM70, or HIBADH esiRNA for 48 h followed by infection with type II:MAF1b parasites (MOI 2). At 24 hpi, cells were fixed with 2.5% glutaraldehyde in PBS overnight at 4 °C and then washed three times with PBS for 10 min, postfixed for 1 h at 4 °C in 1% OsO_4 with 1% potassium ferricyanide, and washed three times with PBS. Samples were then dehydrated in a graded series of alcohol for 10 min with three changes in 100% ethanol for 15 min and changed three times in Epon for 1 h each. Following the removal of Epon, samples were covered with resin and polymerized at 37 °C overnight and then for 48 h at 60 °C (protocol: Center for Biological Imagining [CBI], University of Pittsburgh). Samples were sectioned and processed by the CBI and imaged on a JEOL JEM 1011 transmission electron microscope at 80 kV fitted with a bottom-mount AMT 2k digital camera (Advanced Microscopy Techniques). Five vacuoles containing two parasites were imaged for each of the infections. Vacuoles were traced in ImageJ and the percent of the total distance around the vacuole in direct contact with the host mitochondria was quantified for each of the mutants and controls. A minimum of 19 vacuoles for each esiRNA treatment were imaged. Vacuoles were traced in FIJI ImageJ and the percent of the total distance around the vacuole in contact with the host mitochondria was quantified for each esiRNA treatment group. Quantification and statistical analyses were performed in Prism.

ER Visualization Experiments. U2OS-mCherry cells were infected with type II:MAF1a/b at an MOI of 1.5 and fixed at 24 hpi. Immunofluorescence assays were performed as listed above using anti-mitochondria and anti-HA antibodies. A profile line was chosen in FIJI ImageJ (NIH) in the MAF1-only channel and subsequently overlaid with the ER and mitochondria channels to develop profile plots. Images were pseudocolored as described above.

Immunoprecipitation and Quantitative Mass Spectrometry. HFFs were seeded to confluency in a T175 flask (107 cells) and hyperinfected (MOI 10) with either type II:MAF1b, type II:MAF1a, or type II:MAF1b mutant parasites ($n = 7$) for 24 h. Cell were lysed in IP lysis buffer (50 mM Tris, pH 8.0, 150 mM NaCl, 1% IGEPAL CA-630, and 0.05% Tween 20) supplemented with cOmplete ULTRA tablet protease inhibitors (Roche) on ice. Following sonication using three 15-mV 10-s bursts with 25-s intervals on ice, the insoluble fraction was pelleted at 800 × *g* for 10 min at 4 °C. The soluble fraction was incubated with Pierce anti-HA magnetic beads (Thermo Fisher) overnight using a rotator. Beads were washed five times with IP lysis buffer and eluted by boiling in SDS sample buffer (Thermo Fisher). Eluate fractions were resolved at 150 V for 10 min by 10% SDS-PAGE to only allow the protein samples to enter the resolving portion of the gel. The eluted samples were loaded onto a 4 to 12% Bis-Tris gradient gel in ∼18-μL aliquots at constant 150 V, 1× (2-(*N*-morpholino)ethanesulfonic acid) buffer for 2 min or until the entire sample was loaded. The gel bands were digested with trypsin as described (44) and tryptic peptides were desalted with Pierce C18 spin columns, SpeedVac-dried, and resuspended in 18 μL 0.1% formic acid. A pooled instrument control was made by taking 3 μL from each of the 21 replicate samples. The injection order was randomized in a balanced block design.

All samples were analyzed by nanoflow liquid chromatography tandem mass spectrometry (nLC-MS/MS) using an injection volume of 1 μL onto a 25-cm C18 PicoChip column. The LC gradient ran at 300 nL/min with 2 to 35% acetonitrile over a 66-min gradient. Instrument parameters included a full scan with top13 ddMS2 on the high-resolution Thermo Orbitrap Velos Pro mass spectrometer.

Extracted ion chromatogram peak areas for 32 selected peptides were monitored during the instrumental analysis to ensure proper instrument performance using Skyline software. A MASCOT database search was performed using a modified UniProt human database with a *T. gondii* protein sequence database with the parameters fixed-modification carbamidomethylation (C) and variable modifications of acetyl (N terminus), oxidation (M), and deamidation (NQ). Major identified proteins were reported in Scaffold v4.5.3. Proteomic features were aligned and quantitated using

MaxQuant v1.6.2.1 software and the Andromeda search engine with 1% false discovery rate selected. GraphPad Prism was used to create bar charts. Matlab was used for the statistical analysis. The mass spectrometry proteomics data have been deposited in the ProteomeXchange Consortium via the Proteomics Identification Database (PRIDE) (45) partner repository with the dataset identifier PXD023485.

Recombinant Cloning, Protein Production, and Purification.

TgMAF1a and TgMAF1b. Clones encoding amino acids T159 to D435 of *Tg*MAF1a and S173 to D443 of *Tg*MAF1b were codon-optimized for expression in *Escherichia coli* and synthesized by GenScript. Genes were subcloned into an engineered vector encoding a tobacco etch virus (TEV) protease-cleavable N-terminal hexahistidine tag. MAF1 constructs were expressed in BL21 cells overnight at 30 °C, and purified with Ni-affinity chromatography. Proteins were further purified using size-exclusion chromatography (SEC) with a Superdex 75 16/600 column in 20 mM Hepes (pH 8.0), 150 mM NaCl, and 1 mM dithiothreitol (DTT).

TOM70. Clones encoding amino acids N109 to A598 of human TOM70 (accession no. NP_055635.3) were codon-optimized for expression in insect cells and synthesized by GenScript. Genes were subcloned into a modified pAcGP67b vector (Pharmingen) encoding a TEV protease-cleavable N-terminal twin-strep-II tag. TOM70 was expressed in *Tni* cells. After 72 h, the cells were removed by centrifugation and the supernatant was concentrated and buffer-exchanged using a tangential flow system with a 10-kDa filter. TOM70 was then purified with streptavidin-affinity chromatography, and cleaved overnight with TEV protease. TOM70 was further purified using SEC with a Superdex 75 16/600 column in 20 mM Hepes (pH 7.5), 150 mM NaCl, and 1 mM DTT.

Recombinant protein pull-down assay. TOM70 (350 μg) was combined with 20 μL Ni^{2+}-Sepharose beads and 40 μg (5× molar ratio) of *Tg*MAF1a, *Tg*MAF1b, or nothing (negative control) and filled to 500 μL with Ni^{2+} binding buffer (20 mM Hepes, pH 8.0, 50 mM imidazole, 1 M NaCl, and 2 mM 2-beta-mercaptoethanol [BME]). Pull-downs were incubated for 1 h with rotation at 4 °C. Ni^{2+}-Sepharose beads were then centrifuged and the supernatant was removed, and the beads were washed three times with 500 μL of Ni^{2+} binding buffer. Bound protein was then eluted from the beads using 30 μL of Ni^{2+} stripping buffer (20 mM Hepes, pH 8.0, 500 mM imidazole, 1 M NaCl, and 2 mM BME), 20 μL of which was then loaded on a 12% SDS-PAGE gel.

MAF1 Ectopic Expression. U2OS cells were plated to 80% confluency and transfected with 1 μg of GFP-MAF1b/a plasmid by lipofection (Lipofectamine 3000). In some cases, U2OS cells were treated with 25 nM target esiRNA for 48 h followed by transfection with 1 μg of GFP-MAF1b/a plasmid for 24 h. Following transfection, cells were fixed and stained with anti-mitochondria antibody for immunofluorescence analysis. Additionally, VDAC2 localization was investigated by transfecting both GFP-MAF1a/b for 24 h followed by fixation and immunofluorescence analysis. Ectopic expression of GFP-MAF1a/b and immunofluorescence after treatment with esiRNAs were performed as outlined above. To quantify colocalization signal, Manders' overlap coefficient was calculated using the JACoP plugin for ImageJ (46).

iMT TargetP Analysis. Both *Tg*MAF1RHa1 (MAF1a) and *Tg*MAF1RHb2 (MAF1b) sequences were subjected to TargetP prediction software as described (18). The algorithm N-terminally truncates the protein of interest by a single residue at a time and assigns a score to the truncated form. This allowed us to identify regions of *Tg*MAF1b/a that are predicted iMTSs.

TOM70 and VDAC2 Enrichment. Mito-RFP NRK cells were infected with either type II:MAF1a or type II:MAF1b parasites (MOI 2). Mito-RFP NRK cells were fixed at 24 hpi and stained for the HA tag and TOM70 or VDAC2 (antibodies previously described). Using FIJI ImageJ software, the raw intensity density of a 15 × 15-pixel area was measured in a region on the PVM and off of the PVM. An enrichment ratio was calculated (pixel intensity on the PVM/pixel intensity off of the PVM) in both the RFP-mitochondria channel and the TOM70/VDAC2 channel (three biological replicates).

To determine if infection led to stabilization of TOM70, we seeded U2OS cells in a 24-well plate until they reached confluency. Wells were infected with type II:MAF1b or type II:MAF1a or uninfected at an MOI of 5 (n = 3 per treatment condition). Cells were lysed at 24 h after infection in Pierce IP lysis buffer (Thermo Fisher) and treated with cOmplete protease inhibitors (Roche) on ice. Samples were boiled in SDS sample buffer for 10 min, resolved by 10% SDS-PAGE, and transferred to a nitrocellulose membrane. Membranes were blocked in 5% BSA in PBST and probed with primary antibodies to TOM70, β-actin, and VDAC2 followed by HRP-conjugated secondary antibodies. Membranes were visualized with SuperSignal West Femto chemiluminescent substrates. Antibodies used for these experiments were as follows: anti-TOM70 (sc-390545; Santa Cruz Biotechnology), anti–β-actin (4970; Cell Signaling Technology), anti-VDAC2 (PA5-28106; Thermo Fisher), goat anti-rabbit IgG HRP (Southern Biotech), and goat anti-mouse IgG HRP (Southern Biotech).

Data Availability. Proteomics data reported in this article have been deposited in the Proteomics Xchange/PRIDE Consortium (accession no. PXD023485).

ACKNOWLEDGMENTS. We thank Dr. Carolyn Coyne (University of Pittsburgh School of Medicine) for providing KDEL-mCherry cells, Dr. Mitch Ellison (University of Pittsburgh Department of Biological Sciences) for help with R scripts, and Dr. Mike Panas, Dr. Felice Kelly, and Dr. John Boothroyd (Stanford University) for sharing preliminary unpublished data while this work was ongoing. Portions of this manuscript were developed in the PhD thesis of M.L.B. (2020).

1. M. A. Horwitz, Formation of a novel phagosome by the Legionnaires' disease bacterium (*Legionella pneumophila*) in human monocytes. *J. Exp. Med.* **158**, 1319–1331 (1983).
2. A. Matsumoto, H. Bessho, K. Uehira, T. Suda, Morphological studies of the association of mitochondria with chlamydial inclusions and the fusion of chlamydial inclusions. *J. Electron Microsc. (Tokyo)* **40**, 356–363 (1991).
3. A. Matsumoto, Isolation and electron microscopic observations of intracytoplasmic inclusions containing *Chlamydia psittaci*. *J. Bacteriol.* **145**, 605–612 (1981).
4. Y. Adomako-Ankomah *et al*., Host mitochondrial association evolved in the human parasite *Toxoplasma gondii* via neofunctionalization of a gene duplicate. *Genetics* **203**, 283–298 (2016).
5. J. P. Dubey, C. Sreekumar, Redescription of *Hammondia hammondi* and its differentiation from *Toxoplasma gondii*. *Int. J. Parasitol.* **33**, 1437–1453 (2003).
6. L. Pernas *et al*., *Toxoplasma* effector MAF1 mediates recruitment of host mitochondria and impacts the host response. *PLoS Biol.* **12**, e1001845 (2014).
7. M. L. Blank *et al*., A *Toxoplasma gondii* locus required for the direct manipulation of host mitochondria has maintained multiple ancestral functions. *Mol. Microbiol.* **108**, 519–535 (2018).
8. D. M. Ojcius, H. Degani, J. Mispelter, A. Dautry-Varsat, Enhancement of ATP levels and glucose metabolism during an infection by *Chlamydia*. NMR studies of living cells. *J. Biol. Chem.* **273**, 7052–7058 (1998).
9. N. Radomski, R. Einenkel, A. Müller, M. R. Knittler, *Chlamydia*-host cell interaction not only from a bird's eye view: Some lessons from *Chlamydia psittaci*. *FEBS Lett.* **590**, 3920–3940 (2016).
10. P. Escoll *et al*., *Legionella pneumophila* modulates mitochondrial dynamics to trigger metabolic repurposing of infected macrophages. *Cell Host Microbe* **22**, 302–316.e7 (2017).
11. E. D. English, J. P. Boyle, Impact of engineered expression of mitochondrial association factor 1b on *Toxoplasma gondii* infection and the host response in a mouse model. *mSphere* **3**, e00471-18 (2018).
12. L. Pernas, J. C. Boothroyd, Association of host mitochondria with the parasitophorous vacuole during *Toxoplasma* infection is not dependent on rhoptry proteins ROP2/8. *Int. J. Parasitol.* **40**, 1367–1371 (2010).
13. Y. Adomako-Ankomah, G. M. Wier, A. L. Borges, H. E. Wand, J. P. Boyle, Differential locus expansion distinguishes *Toxoplasmatinae* species and closely related strains of *Toxoplasma gondii*. *mBio* **5**, e01003-13 (2014).
14. F. D. Kelly *et al*., *Toxoplasma gondii* MAF1b binds the host cell MIB complex to mediate mitochondrial association. *mSphere* **2**, e00183-17 (2017).
15. A. K. Heninger, F. Buchholz, Production of endoribonuclease-prepared short interfering RNAs (esiRNAs) for specific and effective gene silencing in mammalian cells. *CSH Protoc.* **2007**, pdb.prot4824 (2007).
16. A. M. Edmonson, D. K. Mayfield, V. Vervoort, B. R. DuPont, G. Argyropoulos, Characterization of a human import component of the mitochondrial outer membrane, TOMM70A. *Cell Commun. Adhes.* **9**, 15–27 (2002).
17. H. Yamamoto *et al*., Roles of Tom70 in import of presequence-containing mitochondrial proteins. *J. Biol. Chem.* **284**, 31635–31646 (2009).
18. S. Backes *et al*., Tom70 enhances mitochondrial preprotein import efficiency by binding to internal targeting sequences. *J. Cell Biol.* **217**, 1369–1382 (2018).
19. E. M. Manders, J. Stap, G. J. Brakenhoff, R. van Driel, J. A. Aten, Dynamics of three-dimensional replication patterns during the S-phase, analysed by double labelling of DNA and confocal microscopy. *J. Cell Sci.* **103**, 857–862 (1992).
20. M. Colombini, The VDAC channel: Molecular basis for selectivity. *Biochim. Biophys. Acta* **1863**, 2498–2502 (2016).
21. S. Naghdi, G. Hajnóczky, VDAC2-specific cellular functions and the underlying structure. *Biochim. Biophys. Acta* **1863**, 2503–2514 (2016).
22. I. Coppens, J. D. Romano, Hostile intruder: *Toxoplasma* holds host organelles captive. *PLoS Pathog.* **14**, e1006893 (2018).
23. M. L. Blank, J. P. Boyle, Effector variation at tandem gene arrays in tissue-dwelling coccidia: Who needs antigenic variation anyway? *Curr. Opin. Microbiol.* **46**, 86–92 (2018).

MICROBIOLOGY

24. T. Bausewein *et al*., Cryo-EM structure of the TOM core complex from *Neurospora crassa*. *Cell* **170**, 693–700.e7 (2017).
25. D. Rapaport, Biogenesis of the mitochondrial TOM complex. *Trends Biochem. Sci.* **27**, 191–197 (2002).
26. R. Filadi *et al*., TOM70 sustains cell bioenergetics by promoting IP3R3-mediated ER to mitochondria Ca^{2+} transfer. *Curr. Biol.* **28**, 369–382.e6 (2018).
27. A. P. West, G. S. Shadel, S. Ghosh, Mitochondria in innate immune responses. *Nat. Rev. Immunol.* **11**, 389–402 (2011).
28. A. J. Anderson, T. D. Jackson, D. A. Stroud, D. Stojanovski, Mitochondria-hubs for regulating cellular biochemistry: Emerging concepts and networks. *Open Biol.* **9**, 190126 (2019).
29. S. Missiroli *et al*., Mitochondria-associated membranes (MAMs) and inflammation. *Cell Death Dis.* **9**, 329 (2018).
30. J. Rieusset, The role of endoplasmic reticulum-mitochondria contact sites in the control of glucose homeostasis: An update. *Cell Death Dis.* **9**, 388 (2018).
31. J. Melin *et al*., A presequence-binding groove in Tom70 supports import of Mdl1 into mitochondria. *Biochim. Biophys. Acta* **1853**, 1850–1859 (2015).
32. X. Liu *et al*., An AP-MS- and BioID-compatible MAC-tag enables comprehensive mapping of protein interactions and subcellular localizations. *Nat. Commun.* **9**, 1188 (2018).
33. J. C. Young, N. J. Hoogenraad, F. U. Hartl, Molecular chaperones Hsp90 and Hsp70 deliver preproteins to the mitochondrial import receptor Tom70. *Cell* **112**, 41–50 (2003).
34. Y. Shan, G. Cortopassi, Mitochondrial Hspa9/mortalin regulates erythroid differentiation via iron-sulfur cluster assembly. *Mitochondrion* **26**, 94–103 (2016).
35. M. A. Huynen, M. Mühlmeister, K. Gotthardt, S. Guerrero-Castillo, U. Brandt, Evolution and structural organization of the mitochondrial contact site (MICOS) complex and the mitochondrial intermembrane space bridging (MIB) complex. *Biochim. Biophys. Acta* **1863**, 91–101 (2016).
36. S. Liu *et al*., Phosphorylation of innate immune adaptor proteins MAVS, STING, and TRIF induces IRF3 activation. *Science* **347**, aaa2630 (2015).
37. X. Y. Liu, B. Wei, H. X. Shi, Y. F. Shan, C. Wang, Tom70 mediates activation of interferon regulatory factor 3 on mitochondria. *Cell Res.* **20**, 994–1011 (2010).
38. S. S. Guan, M. L. Sheu, C. T. Wu, C. K. Chiang, S. H. Liu, ATP synthase subunit-β down-regulation aggravates diabetic nephropathy. *Sci. Rep.* **5**, 14561 (2015).
39. X. Fu *et al*., 2-Hydroxyglutarate inhibits ATP synthase and mTOR signaling. *Cell Metab.* **22**, 508–515 (2015).
40. E. J. Melo, W. de Souza, Relationship between the host cell endoplasmic reticulum and the parasitophorous vacuole containing *Toxoplasma gondii*. *Cell Struct. Funct.* **22**, 317–323 (1997).
41. A. P. Sinai, P. Webster, K. A. Joiner, Association of host cell endoplasmic reticulum and mitochondria with the *Toxoplasma gondii* parasitophorous vacuole membrane: A high affinity interaction. *J. Cell Sci.* **110**, 2117–2128 (1997).
42. K. Mitra, J. Lippincott-Schwartz, Analysis of mitochondrial dynamics and functions using imaging approaches. *Curr. Protoc. Cell Biol.* **46**, 4.25.1–4.25.21 (2010).
43. J. E. Lee, H. Yuan, F. X. Liang, P. B. Sehgal, Nitric oxide scavenging causes remodeling of the endoplasmic reticulum, Golgi apparatus and mitochondria in pulmonary arterial endothelial cells. *Nitric Oxide* **33**, 64–73 (2013).
44. A. Braganza *et al*., UBE3B is a calmodulin-regulated, mitochondrion-associated E3 ubiquitin ligase. *J. Biol. Chem.* **292**, 2470–2484 (2017).
45. Y. Perez-Riverol *et al*., The PRIDE database and related tools and resources in 2019: Improving support for quantification data. *Nucleic Acids Res.* **47**, D442–D450 (2019).
46. S. Bolte, F. P. Cordelières, A guided tour into subcellular colocalization analysis in light microscopy. *J. Microsc.* **224**, 213–232 (2006).